

A novel crystal-analyzer phase retrieval algorithm and its noise property

Yuan Bao,^{a,b} Yan Wang,^b Panyun Li,^b Zhao Wu,^a Qigang Shao,^a Kun Gao,^a Zhi Wang,^a Zaiqiang Ju,^b Kai Zhang,^b Qingxi Yuan,^b Wanxia Huang,^b Peiping Zhu^{a,b,c,*} and Ziyu Wu^{a,b*}

Received 18 December 2014

Accepted 21 February 2015

Edited by A. Momose, Tohoku University, Japan

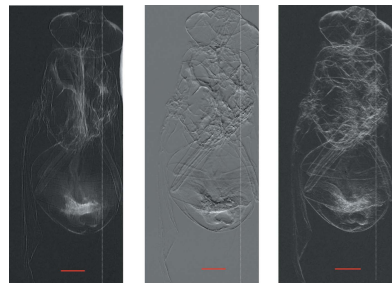
Keywords: diffraction enhanced imaging; phase retrieval; noise in imaging systems.

^aNational Synchrotron Radiation Laboratory, University of Science and Technology of China, Hefei, Anhui 230029, People's Republic of China, ^bInstitute of High Energy Physics, Chinese Academy of Science, Beijing 100049, People's Republic of China, and ^cBeijing Center for Mathematics and Information Interdisciplinary Sciences, Beijing 100048, People's Republic of China. *Correspondence e-mail: zhupp@ihep.ac.cn, wuzy@ustc.edu.cn

A description of the rocking curve in diffraction enhanced imaging (DEI) is presented in terms of the angular signal response function and a simple multi-information retrieval algorithm based on the cosine function fitting. A comprehensive analysis of noise properties of DEI is also given considering the noise transfer characteristic of the X-ray source. The validation has been performed with synchrotron radiation experimental data and Monte Carlo simulations based on the *Geant4* toolkit combined with the refractive process of X-rays, which show good agreement with each other. Moreover, results indicate that the signal-to-noise ratios of the refraction and scattering images are about one order of magnitude better than that of the absorption image at the edges of low-Z samples. The noise penalty is drastically reduced with the increasing photon flux and visibility. Finally, this work demonstrates that the analytical method can build an interesting connection between DEI and GDPCI (grating-based differential phase contrast imaging) and is widely suitable for a variety of measurement noise in the angular signal response imaging prototype. The analysis significantly contributes to the understanding of noise characteristics of DEI images and may allow improvements to the signal-to-noise ratio in biomedical and material science imaging.

1. Introduction

Diffraction enhanced imaging (DEI), also referred to as analyzer-based imaging (ABI), produces three images, each one associated with absorption, refraction and ultra-small-angle X-ray scattering (USAXS). The technique was pioneered by Förster (Förster *et al.*, 1980) more than three decades ago, but became a competitive phase contrast imaging method only in the last decade (Chapman *et al.*, 1997; Bravin, 2003; Thominson *et al.*, 2005; Zhu *et al.*, 2005; Zhang *et al.*, 2010; Diemoz *et al.*, 2010; Sumitani *et al.*, 2013). In DEI the sample is set between a monochromator crystal and an analyzer crystal. The monochromator crystal works as an angular collimator with an acceptance angle of a few micro-radians, while the analyzer crystal acts as a narrow angular band-pass filter with the same high angular sensitivity. Each pixel of a detector behind the analyzer crystal measures the angular response. When the analyzer crystal rotates with respect to the monochromator crystal, the so-called rocking curve (RC) function can be measured. Since the angular deviation caused by the sample is equivalent to that caused by a rotation of the analyzer crystal, the recorded image contains the angular information about each point of the sample. Thanks to the presence of the analyzer crystal, the contrast of



© 2015 International Union of Crystallography

images collected with a DEI setup is at least an order of magnitude better than the contrast of the same object collected with a conventional absorption imaging method (Chapman *et al.*, 1997).

Actually the acronym DEI was introduced by Chapman *et al.* (1997) with particular regard to a geometrical optics-based algorithm. The latter combines the two half-slope images decoupling refraction from extinction (rejection of small- and ultra-small-angle scattering) and absorption. But the USAXS is ignored in Chapman's algorithm. In order to compensate for the shortcomings of Chapman's algorithm, several approaches have been proposed in the last decade. A modified algorithm collecting two images at two different defined angles along the RC was proposed by Rigon *et al.* (2003). However, this algorithm took care of absorption and USAXS effects only, and could not retrieve refraction information. Another method known as multiple-image radiography (MIR) was proposed by Wernick (Wernick *et al.*, 2003; Khelashvili *et al.*, 2006). In this case the radiative transport theory was used to model the X-ray field propagation. It showed that MIR truly separated absorption, refraction and USAXS, and all three MIR images were virtually immune to degradation caused by scattering at higher angles. Moreover, Chou *et al.* (2007) developed an extended DEI method (E-DEI) for concurrent reconstruction of three images representing the projected X-ray absorption, refraction and USAXS properties of the sample. The E-DEI method successfully circumvented the limitations of the classic or scattering-based (S-B) DEI imaging models by merging the two models. It can be considered as an implementation of the MIR paradigm. In analogy to MIR, Pagot *et al.* (2003) used a statistical method for the RC and evaluated parametric images based on its zeroth-, first- and second-order moments and on the maximum of the RC. In addition, Nesterets *et al.* (2006) proposed an alternative method that utilized Gaussian curves to fit the reference and object RCs. Although up to now MIR is considered as the gold standard method, it delivers large radiation doses due to a multiple exposure procedure. As an alternative to MIR, although with some limitations, Rigon *et al.* (2007a,b) proposed a simpler algorithm to retrieve absorption, differential phase and scattering signal considering only three images, and extended it into hard X-ray grating interferometry (Pelliccia *et al.*, 2013).

Following Chapman's classical framework, we proposed a different approach in which the RC can be treated as the angular signal response function. Based on the angular signal response prototype, DEI has been developed optimizing one of the two feasible approaches. The first approach considered the intrinsic RC as an angular signal response function, and the detected image can be expressed as the convolution between the sample angular function and the intrinsic RC. The second approach was based on a double-wave detection, which collected absorption, refraction and scattering information by comparison of the full RC modulated by the sample with the intrinsic RC. Chapman's algorithm belonged to the first, while the Gaussian curve fitting method (Nesterets *et al.*, 2006) and the methods proposed by Oltulu (2003) and Wernick *et al.* (2003) belonged to the second.

DEI not only introduced refraction and scattering information for radiography (Oltulu, 2003) but also triggered the development of other phase contrast imaging methods (Zhu *et al.*, 2010; Munro & Olivo, 2013). In particular, as a reference model, its conclusion can be generalized to many collimator-analyzer-based imaging methods (Zhu *et al.*, 2014). Although DEI has been developed for more than a decade, many research issues still need to be clarified and improved. For instance, Wernick *et al.* (Brankov *et al.*, 2004) presented a noise analysis of Chapman's classical algorithm; however, it neglected errors due to the bias of the analyzer crystal. Marquet *et al.* (2006) investigated the noise properties of MIR by deriving the Cramér-Rao lower bound (CRLB) for the absorption, refraction and scattering images. Assuming a fixed radiation dose delivered to an object, Majidi *et al.* (2014) used the CRLB to quantify the noise properties in estimated images and to investigate the effect of source intensity, different analyzer-crystal angular positions and object properties on this bound. Pagot *et al.* (2005) presented a comparative study of DEI and PPI (phase propagation imaging) techniques in a quantitative way for mammography applications. Other works have also been published (Weber *et al.*, 2011a,b; Chen *et al.*, 2011; Diemoz *et al.*, 2012; Li *et al.*, 2013; Rizzi *et al.*, 2013; Tang *et al.*, 2011, 2012) regarding the noise analysis of grating-based differential phase contrast imaging (GDPCI). Revol *et al.* (2010) developed a quantitative description of the stochastic error in GDPCI, and Weber *et al.* (2011a) introduced a least-squares fitting algorithm in the matrix notation to calculate the noise behaviour of absorption, differential phase and scattering images [also called dark-field images in GDPCI (Pfeiffer *et al.*, 2008; Wang *et al.*, 2009a)].

Recently, based on the angular signal response prototype, we introduced a new method using a cosine function to fit the intrinsic RC (Zhao *et al.*, 2013). Thanks to the symmetry of the cosine function, collecting three measurements at three symmetric points on the cosine function, the method may extract absorption, refraction and USAXS images. This approach provides a simple and fast method to retrieve information and establishes a straightforward relationship between DEI and GDPCI, which further supports and complements the conclusion given by Pelliccia *et al.* (2013). Meanwhile, based on the angular signal response imaging prototype, a comprehensive analysis of the noise behaviour of the three images, *i.e.* absorption, refraction and USAXS, is lacking for DEI.

2. Background

2.1. Principles of diffraction enhanced imaging

To separate and extract the independent images of an object, *i.e.* absorption, refraction and USAXS, we set up the imaging layout based on the angular collimator-analyzer layout shown in Fig. 1.

In Fig. 1, we have shown the schematic DEI layout and the corresponding RC, which describes the reflected intensity of the analyzer crystal without the sample *versus* the rocking

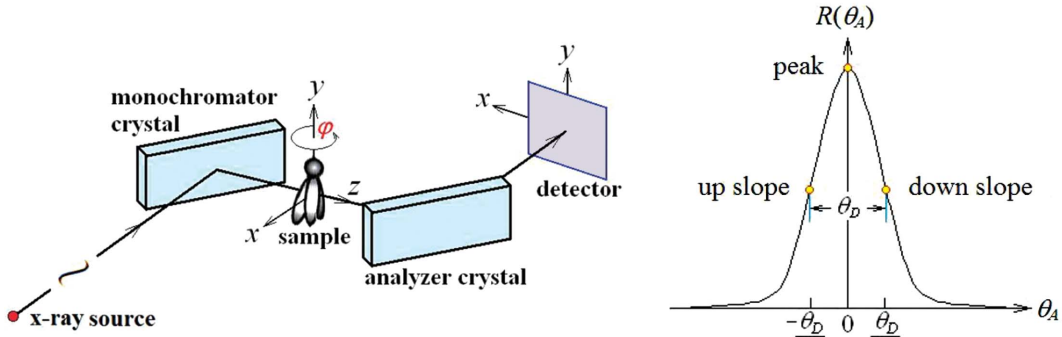


Figure 1
Experimental layout for diffraction enhanced imaging and its RC.

angle θ_A between the analyzer and the monochromator crystals. The photon number I recorded in the detector plane can be written as

$$I_{\theta_A} = I_0 At R(\theta_A), \quad (1)$$

where I_0 is the flux of the incident radiation in the sample plane, $R(\theta_A)$ is the reflectivity, also called the rocking curve, a function of the analyzer's rotation angle θ_A ; A is the detector pixel area and t the exposure time.

When a sample is placed in the X-ray beam, between the monochromator and the analyzer crystals, it will absorb, refract and scatter the X-ray radiation going through the sample. The object function can be expressed as (Khelashvili *et al.*, 2006; Chou *et al.*, 2007; Jensen *et al.*, 2010)

$$O(\vartheta; x, y) = I_0 At \frac{\exp[-M(x, y)]}{\sqrt{2\pi}\vartheta_s(x, y)} \exp\left\{-\frac{1}{2}\left[\frac{\vartheta - \theta_x(x, y)}{\vartheta_s(x, y)}\right]^2\right\}, \quad (2)$$

where the absorption of the sample point (x, y) is

$$M(x, y) = \int_{-\infty}^{\infty} \mu(x, y, z) dz. \quad (3)$$

$\mu(x, y, z)$ is the linear absorption coefficient; $\theta_x(x, y)$ is the refraction angle of the point (x, y) in the sample plane, perpendicular to the rotation axis of the crystal, whose expression is

$$\theta_x(x, y) = - \int_{-\infty}^{\infty} \frac{\partial \delta(x, y, z)}{\partial x} dz \quad (4)$$

where $\delta(x, y, z)$ is the refractive index decrement; $\vartheta_s^2(x, y)$ is the variance of the scattering angle at the sample point (x, y) , whose expression is

$$\vartheta_s^2(x, y) = \int_{-\infty}^{\infty} \omega(x, y, z) dz \quad (5)$$

where $\omega(x, y, z)$ is the linear scattering coefficient (Khelashvili *et al.*, 2006; Wernick *et al.*, 2003).

According to the theory the detected image is the convolution between the sample function and the angular signal response function (Wernick *et al.*, 2003), so that

$$I(\vartheta; x, y) = O(\vartheta; x, y) \otimes R(\vartheta). \quad (6)$$

Since the $R(\vartheta)$ introduced by Oltulu (2003) and Wernick *et al.* (2003) in 2003 is quite a complex function without a simple analytical expression, equation (6) can hardly be used to obtain the absorption, refraction and USAXS images of an object.

Chapman's algorithm actually utilizes the linear approximation of the slope of the RC,

$$R(\theta_A) \approx \text{tri}\left(\frac{\theta_A}{\theta_D}\right) = \begin{cases} 1 - |\theta_A|/\theta_D, & |\theta_A| \leq \theta_D \\ 0, & \text{otherwise} \end{cases} \quad (7)$$

where $\text{tri}(*)$ is a triangular function and θ_D is the Darwin width, *i.e.* the full width at half-maximum (FWHM) of the RC. Using equation (6) and neglecting the scattering portion in the object function, the absorption and refraction information can be calculated as

$$M(x, y) = \ln \left[\frac{I_U(x, y) + I_D(x, y)}{I_0 At} \right], \quad (8)$$

$$\theta_x(x, y) = \frac{\theta_D I_D(x, y) - I_U(x, y)}{2(I_D(x, y) + I_U(x, y))}, \quad (9)$$

where I_U and I_D are the detected photon number measured at the up-slope and the down-slope of the RC (defined in Fig. 1), respectively.

2.2. Cosine fitting radiography

The theoretical shape of the RC resembles a triangle with a sharp tip. However, less-perfect systems may be more effective for future imaging clinical applications. Indeed, in systems containing a less perfect crystal and noise due to vibration *etc.*, the RC can be reasonably well approximated by a cosine function. Therefore, to extract scattering information we select a cosine function to fit the RC (Zhao *et al.*, 2013), which is different from the existing models presented by Kitchen (Kitchen *et al.*, 2007, 2010) and Hall (Hall *et al.*, 1977). Since the cosine function is one of the simplest elementary functions, it offers many advantages in data sampling and processing. Actually, considering only the upper part of the RC, the cosine function can smoothly replace it. As shown in Fig. 2, the fitted cosine function properly matches the RC at low angles.

However, even though there is a mismatch between them at high angles, the visibilities of the two curves remain unchanged. Moreover, a precise retrieval of the scattering information clarifies the degradation of visibility of the RCs measured with and without sample. As a consequence, equation (1) can be simplified as an analytic form,

$$I_{\theta_A} = I_0 A t \bar{R} \left[1 + V_0 \cos\left(\frac{\pi}{\theta_D} \theta_A\right) \right], \quad (10)$$

where $\bar{R} = (R_{\max} + R_{\min})/2$ is the mean value of the cosine function over a period and $V_0 = (R_{\max} - R_{\min})/(R_{\max} + R_{\min})$ describes the equivalent visibility of the intrinsic RC.

From equations (2), (6) and (10), the imaging equation of the DEI can be written as

$$I_{\theta_A}(x, y) = I_0 A t \bar{R} \exp[-M(x, y)] \times \left(1 + V(x, y) \cos\left(\frac{\pi}{\theta_D} [\theta_A - \theta_x(x, y)]\right) \right), \quad (11)$$

where $V(x, y)$ is the equivalent visibility of the object RC.

Assuming that the angle distribution of the X-rays scattered by the sample follows the Gaussian distribution, and the phase-stepping curve in GDPCI is very similar to the cosine function, then the difference between $V(x, y)$ and V_0 can be regarded as the response to the scattering width signal $\vartheta_s(x, y)$. As a consequence, the correlation between $V(x, y)$ and $\vartheta_s(x, y)$ can be written as (Wang *et al.*, 2009a)

$$V(x, y) = V_0 \exp\left[-\left(\frac{\pi}{\theta_D}\right)^2 \frac{\vartheta_s^2}{2}\right]. \quad (12)$$

Based on the imaging equation (11), while the analyzer crystal rotates to the three defined orientations ($\theta_A = -\theta_D/2, 0, \theta_D/2$), one can, respectively, acquire the up-slope image, the peak image and the down-slope image. They can be written in terms of the photon number as

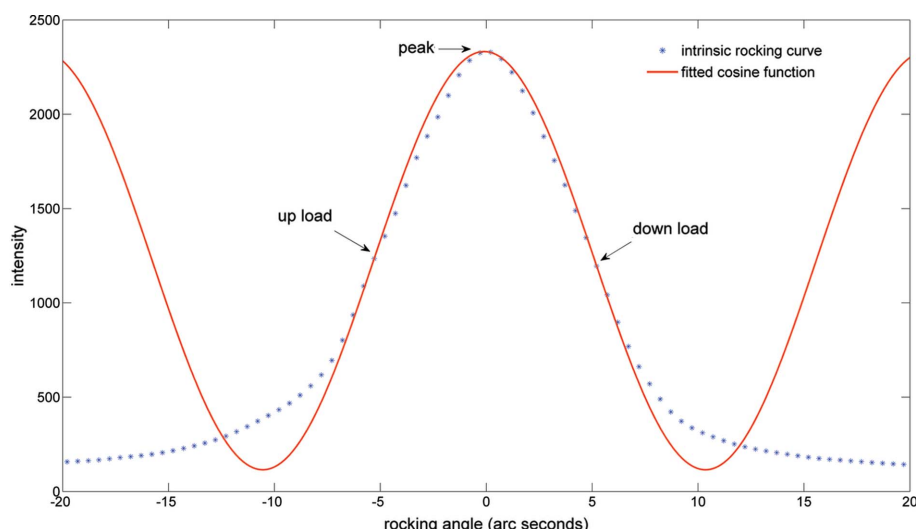


Figure 2

Fit of the intrinsic RC by a cosine function. The up- and down-slope positions refer to the two rocking angles of the analyzer crystal, where the reflectivity is 50% for X-rays that transit the object undeviated, while the peak position corresponds to the maximum of the RC.

$$I_U(x, y) = I_0 A t \bar{R} \exp[-M(x, y)] \left[1 - V(x, y) \sin\left(\frac{\pi}{\theta_D} \theta_x\right) \right], \quad (13)$$

$$I_P(x, y) = I_0 A t \bar{R} \exp[-M(x, y)] \left[1 + V(x, y) \cos\left(\frac{\pi}{\theta_D} \theta_x\right) \right], \quad (14)$$

$$I_D(x, y) = I_0 A t \bar{R} \exp[-M(x, y)] \left[1 + V(x, y) \sin\left(\frac{\pi}{\theta_D} \theta_x\right) \right], \quad (15)$$

where I_U , I_P and I_D are the distribution of photon number recorded in the detector plane corresponding to the defined orientations of the analyzer.

Combining the above three equations, we can easily rewrite

$$T(x, y) = 1 - \exp[-M(x, y)] = 1 - \frac{I_D(x, y) + I_U(x, y)}{2 I_0 A t \bar{R}}, \quad (16)$$

$$\theta_x(x, y) = \frac{\theta_D}{\pi} \arctan \left[\frac{I_D(x, y) - I_U(x, y)}{2 I_P(x, y) - I_D(x, y) - I_U(x, y)} \right], \quad (17)$$

$$\begin{aligned} \vartheta_s^2(x, y) &= 2 \left(\frac{\theta_D}{\pi} \right)^2 \ln \left[\frac{V_0}{V(x, y)} \right] \\ &= 2 \left(\frac{\theta_D}{\pi} \right)^2 \ln \left(V_0 \left\{ \left[\frac{2 I_P(x, y)}{I_D(x, y) + I_U(x, y)} - 1 \right]^2 \right. \right. \\ &\quad \left. \left. + \left[\frac{I_D(x, y) - I_U(x, y)}{I_D(x, y) + I_U(x, y)} \right]^2 \right\}^{-1/2} \right) \end{aligned} \quad (18)$$

Actually, using the intrinsic symmetry of the RC, we greatly reduced the calculation complexity, in particular compared with previous algorithms.

3. Noise behaviour in diffraction enhanced imaging

The noise model mainly considers the noise transfer characteristic of the X-ray source. Due to the statistical fluctuations of the photon number, the absorption coefficient, the refraction angle and the scattering standard deviation will fluctuate around a mean value. As an example, $\theta = \bar{\theta} + \Delta\theta$. Assuming the Poisson statistics in the photon number and using the error propagation (Chen *et al.*, 2011), we may show that the noise variance of the absorption image, the refraction angle and the scattering images is determined by the noise variance $\sigma_{l_k}^2 = \bar{l}_k$ of the measurement taken at each angular position of the analyzer crystal. After some mathematical computations (the

detailed derivation is given in Appendix A) we found that

$$\sigma_T^2 = \frac{\exp(-M)}{2I_0 At\bar{R}}, \quad (19)$$

$$\sigma_\varphi^2 = \frac{1 + 2 \sin^2 \bar{\varphi} + 2V \sin \bar{\varphi} \sin(2\bar{\varphi})}{2I_0 At\bar{R} \exp(-M)V^2}, \quad (20)$$

$$\sigma_{\theta_s^2}^2 = 2 \frac{\theta_D^4 4V \cos^3 \bar{\varphi} + 2(1 + V^2) \cos^2 \bar{\varphi} + 1 - V^2}{I_0 At\bar{R} \exp(-M)V^2}, \quad (21)$$

where $\varphi(x, y) = (\pi/\theta_D)\theta_x(x, y)$.

Looking at equations (19), (20) and (21), we may claim that the noise variances of the refraction angle and the scattering variance are not only related to the detected total photon number but also to the attenuation of the sample and to the equivalent visibility of the RC while the noise variance of the absorption image only relates to the first quantity. Finally, if the refraction angles are small enough, equations (20) and (21) can be simplified as

$$\sigma_\varphi^2 = \frac{1}{2I_0 At\bar{R} \exp(-M)V^2}, \quad (22)$$

$$\sigma_{\theta_s^2}^2 = 2 \frac{\theta_D^4}{\pi^4} \frac{V'}{I_0 At\bar{R} \exp(-M)}, \quad (23)$$

where $V' = 1 + 4/V + 3/V^2$. We can also find that the noise variance of the refraction angle is inversely proportional to the square of the visibility while the square of the scattering width is proportional to V' . Finally, according to equations (19), (20) and (21), we can calculate the signal-to-noise ratio (SNR) of absorption, refraction and scattering information, respectively,

$$\text{SNR}_T = \frac{T}{\sigma_T} = \frac{[1 - \exp(-M)](2I_{\text{total}}\bar{R})^{1/2}}{[\exp(-M)]^{1/2}}, \quad (24)$$

$$\text{SNR}_{\theta_x} = \frac{|\bar{\theta}_x|}{\sigma_\theta} = \frac{(\pi/\theta_D)|\bar{\theta}_x|V[2I_{\text{total}}\bar{R} \exp(-M)]^{1/2}}{[1 + 2 \sin^2 \bar{\varphi} + 2V \sin \bar{\varphi} \sin(2\bar{\varphi})]^{1/2}}, \quad (25)$$

$$\text{SNR}_{\theta_s^2} = \frac{\theta_s^2}{\sigma_{\theta_s^2}^2} = \frac{V[2I_{\text{total}}\bar{R} \exp(-M)]^{1/2} \ln(V_0/V)}{[4V \cos^3 \bar{\varphi} + 2(1 + V^2) \cos^2 \bar{\varphi} + 1 - V^2]^{1/2}}, \quad (26)$$

where $I_{\text{total}} = I_0 At$ is the total photon number of the incident X-ray beam.

4. Experiments and simulations

4.1. Experiments

We carried out DEI experiments at the 4W1A beamline station of the Beijing Synchrotron Radiation Facility (BSRF). The samples were a horse-fly and a cylindrical polymethyl methacrylate (PMMA) partially covered by different layers of filter papers. The horse-fly is a biological system containing a wealth of detailed information, while the cylindrical PMMA is a main refractive material and the filter papers are scattering materials.

A schematic of the experimental set-up is shown in Fig. 1. Two Si (111) crystals were used to monochromatize the incoming beam and to analyze the beam exiting from the object, respectively. X-rays with energy of 15 keV were selected with the monochromator crystal. The detector was a very high resolution X-ray digital camera system (with $7.4 \mu\text{m} \times 7.4 \mu\text{m}$ pixel size) and the angular precision of the crystal rotational stage was 0.1 arcsec. An ion chamber, positioned between analyzer and detector, was used to measure the intensity of the diffracted X-rays exiting from the analyzer crystal. Initially, the RC was measured without the sample. Then, we set the analyzer crystal at three defined orientations and collected the projection images. We used only three images to retrieve the absorption, refraction and scattering images based on the cosine fitting radiography and compared them with the results of multiple-image radiography (Wernick *et al.*, 2003), as illustrated in Fig. 3. From the figures, one can readily recognize that cosine fitting radiography (CFR) results

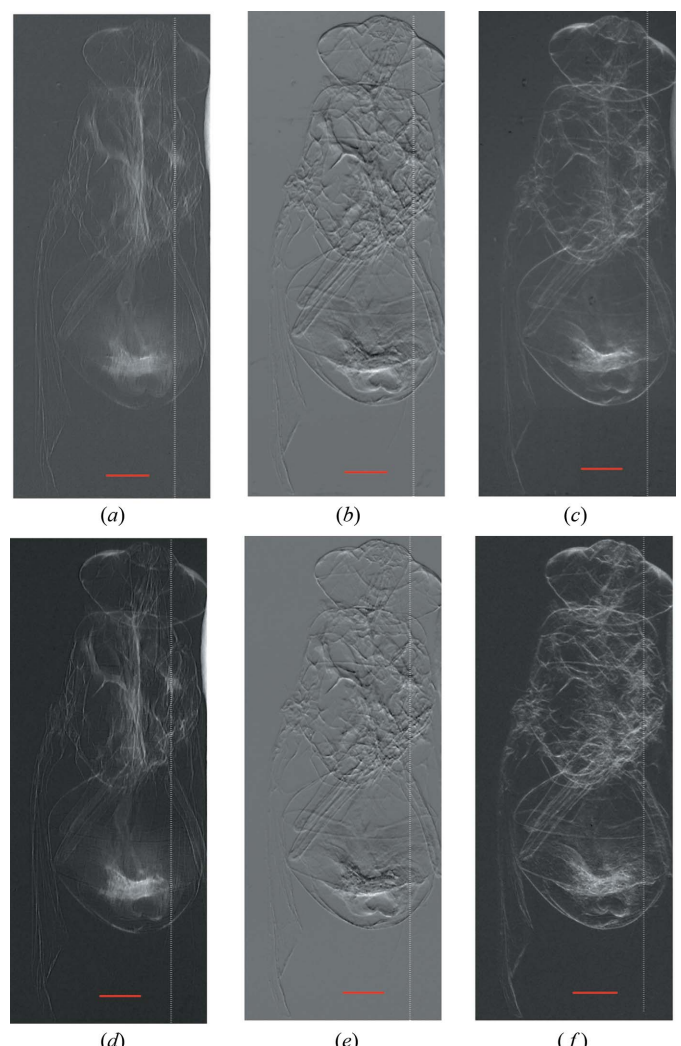
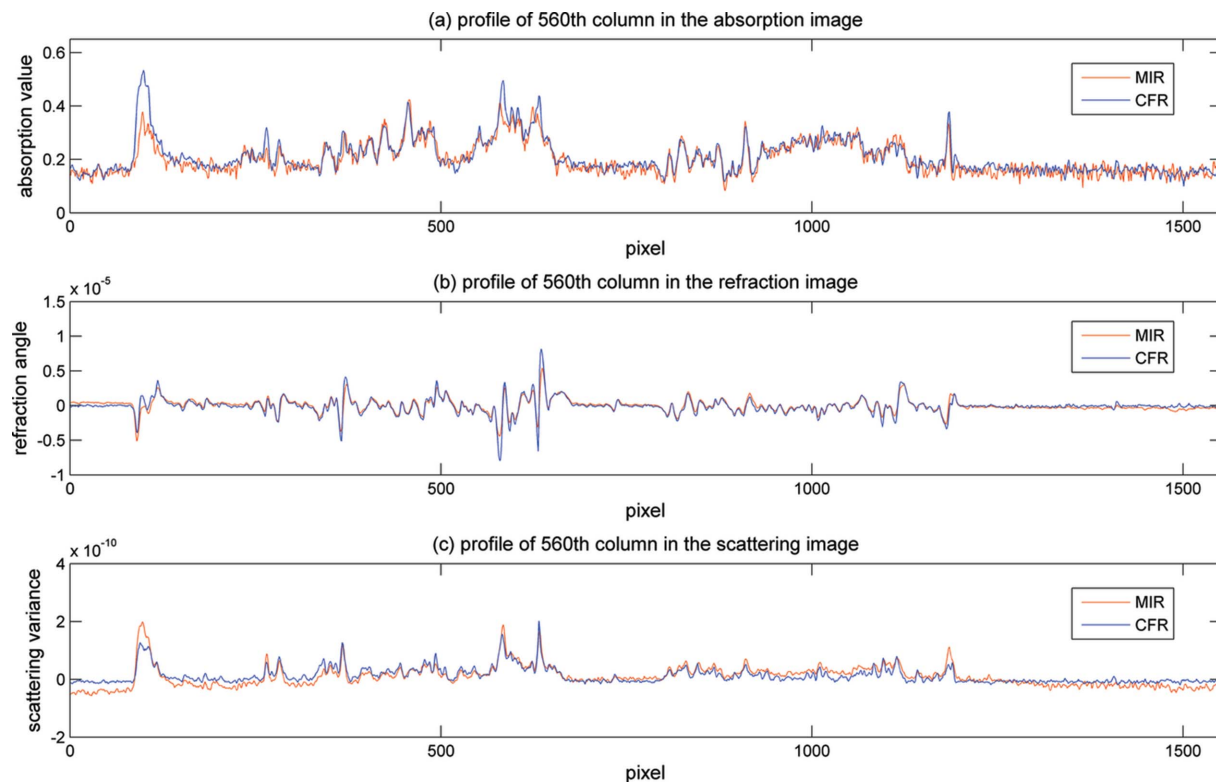


Figure 3
(a–c) Absorption, refraction and scattering images extracted from experimental data with multiple-image radiography (MIR); (d–f) those obtained with cosine fitting radiography (CFR). The red scale bars correspond to 1 mm.

**Figure 4**

The profiles, corresponding to the white lines in Fig. 3, show the comparisons of (a) absorption, (b) refraction and (c) scattering images between CFR and MIR.

are analogous to MIR, as supported by the detailed comparisons shown in Fig. 4 that demonstrates the reliability of this method.

Finally, we used a cylindrical PMMA and filter papers to evaluate the theoretical noise behaviour in DEI described in equations (19), (20) and (21). The papers have a scattering effect reducing the visibility, and their absorption and refraction effects are subordinate. Actually, the papers number increases from one to six and the visibility reduces correspondingly. In Figs. 5–8 experimental results are also compared with Monte Carlo simulations.

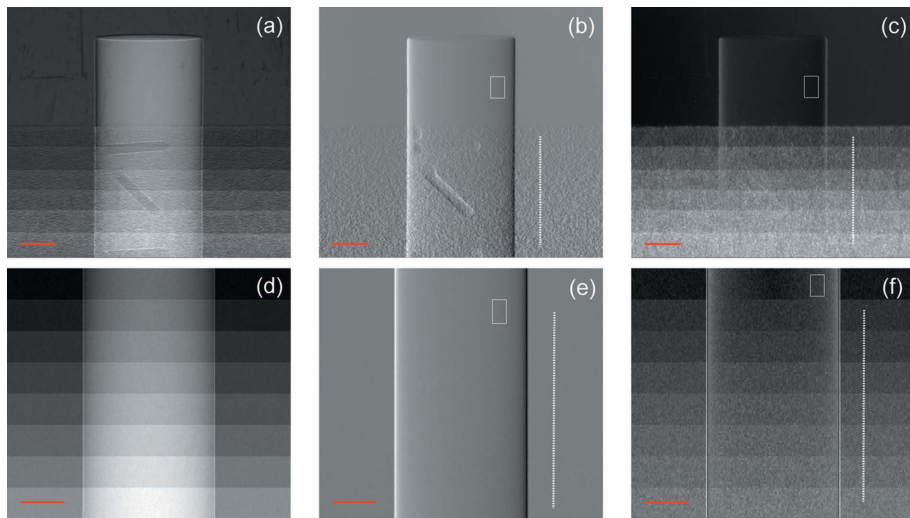
4.2. Simulations

Monte Carlo simulations have been carried out to test the predictions on the noise properties of DEI. These simulations were based on the *Geant4* software (Agostinelli *et al.*, 2003; Allison *et al.*, 2006) which is a toolkit for the simulation of the passage of particles through matter. This *Geant4* toolkit provides a comprehensive set of physics processes to model the behaviour of particles; however, it is not considered appropriate for coherence effects. We introduced the refraction effect in the particle transport process described by Snell's law, adding the capability of phase contrast imaging to *Geant4* (Wang *et al.*, 2009b). We assumed a plane-wave illumination at 15 keV, a specimen made of a PMMA cylinder of 1.5 mm radius and several papers of cellulose. The complex refraction index of the PMMA cylinder is $n = 1 - 1.18 \times 10^{-6}$

$+ i7.59 \times 10^{-10}$ and its density is 1.19 g m^{-3} . In the simulation, we increased the exposure time from 40 ms to more than 100 ms with an increment of about 5 ms. The standard deviations of the refraction angle and the scattering information can be fitted into the curves as a function of the exposure time and the visibility, respectively. Comparison of extracted sample information between simulations and experimental data is shown in Fig. 5 and noise properties in Fig. 6.

Moreover, the SNR is a crucial parameter, which can characterize the sensitivity of an imaging system and lead to the design of a practical experimental setup. We used a cylindrical PMMA to compare the SNR of the absorption, refraction and scattering images described in equations (24), (25) and (26). The results of both experiments and simulations are shown in Fig. 7. It can be seen that the SNR of the absorption image is marked in the middle part of the cylinder, while the SNR of the refraction and scattering images is higher at the edges of the cylinder. The difference may originate from the fact that the edges of the sample play more of a role for refraction and scattering of X-rays than absorption, even though the absorption and scattering of X-rays are both linear with object thickness. Results indicate that refraction and scattering images offer advantages to recognize the edges of an object relative to the conventional absorption-contrast method, especially in biomedical imaging.

The Rose criterion (Bushberg & Boone, 2011) states that a SNR of at least 5 is needed to distinguish image details at

**Figure 5**

(a–c) Absorption, refraction and scattering images extracted from experimental data; (d–f) those of Monte Carlo simulations. In the refraction and scattering images, the noise standard deviations in the white boxes at different exposure times are calculated and compared [Figs. 6(a) and 6(c)], and the noise standard deviations along the white dotted lines with decreasing visibilities are also calculated and compared [Figs. 6(b) and 6(d)]. The red scale bars represent 1 mm.

100% certainty. Based on simulations, we represented the mean intensity in the detector plane with the mean photon number of each pixel, and calculated the SNR at the edge of the sample. The curves are shown in Fig. 8.

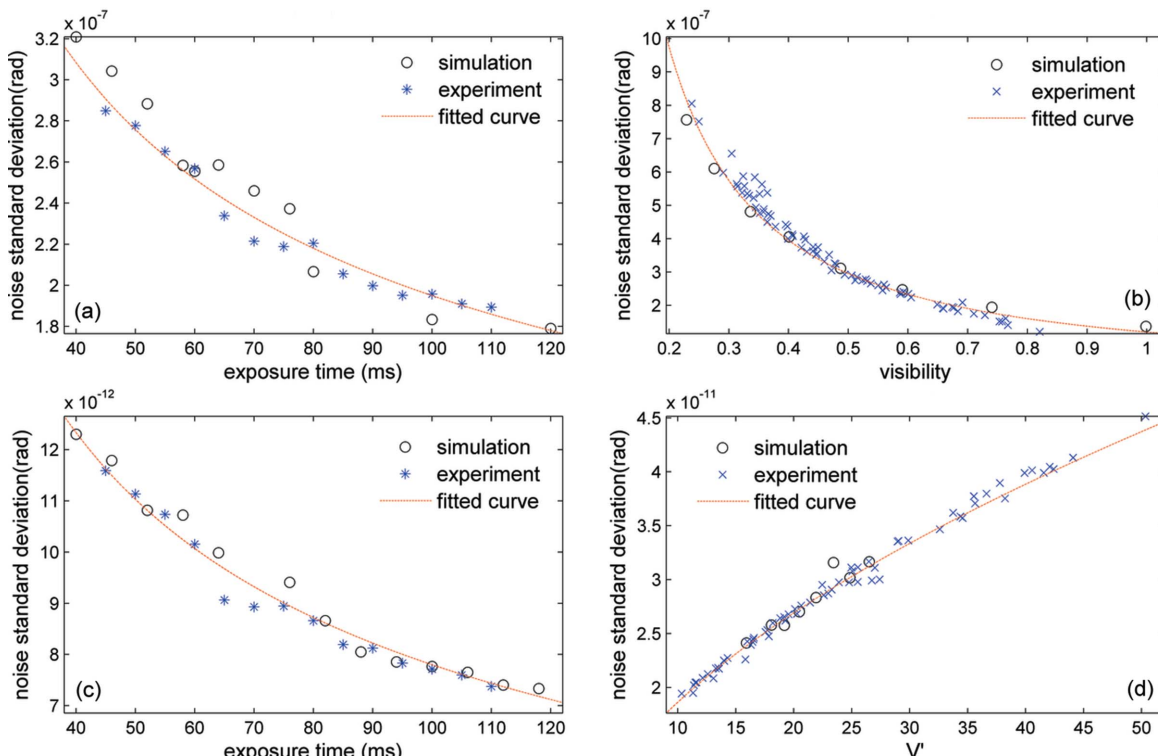
The results of the simulation show that the SNR increases with the average intensity in the detector plane. Even though the mean intensity in the detector plane is only ~ 100 , the SNR

at the edges of the sample is enough for refraction or scattering images compared with an absorption image.

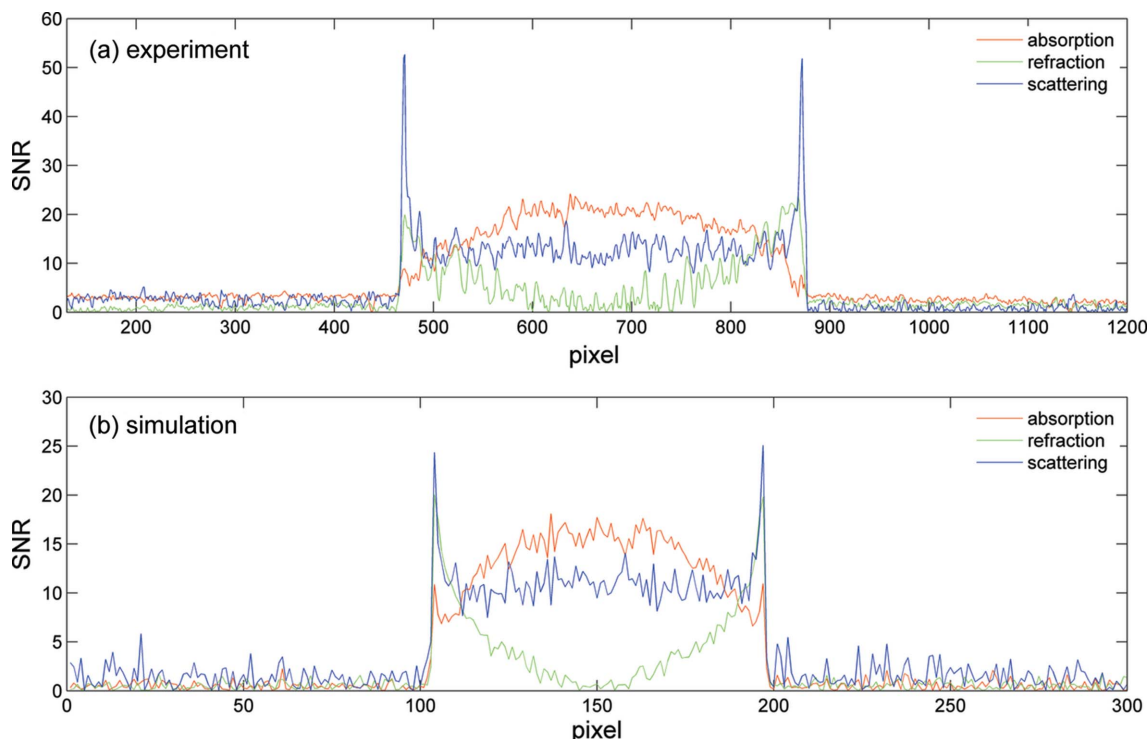
5. Discussion

The refraction and the ultra-small-angle X-ray scattering are both defined as the coherent scattering contributions of X-rays. The former was caused by the density inhomogeneity between adjacent surface elements while the latter within the same surface element. Similarly, they both occur within the resolution elements; however, the refraction of X-rays is regular while the scattering is irregular. Actually, they can be mutually transformed under certain conditions (Zhu *et al.*, 2006). As an example, when the imaging resolution decreases, some refraction X-rays can be treated as USAXS and *vice versa*.

The sources of the detected X-rays can be classified into four cases. Firstly, X-rays impinge on the detector without refraction. Secondly, they are refracted only once. Thirdly, they are refracted more than once toward the same side with respect to the incident direction of the X-rays. Fourthly, they are refracted more than once irregularly toward both sides with respect to the incident direction of the X-rays. In the first three cases, the samples are usually thin enough

**Figure 6**

The standard deviations σ_{θ_1} and σ_{θ_2} plotted *versus* the exposure time and the equivalent visibility of the RC. (a–b) Results of the refraction-angle images; (c–d) results of scattering images.

**Figure 7**

Comparison of the SNR profiles of absorption, refraction and scattering images. (a) and (b) are the results of experiments and simulations, respectively.

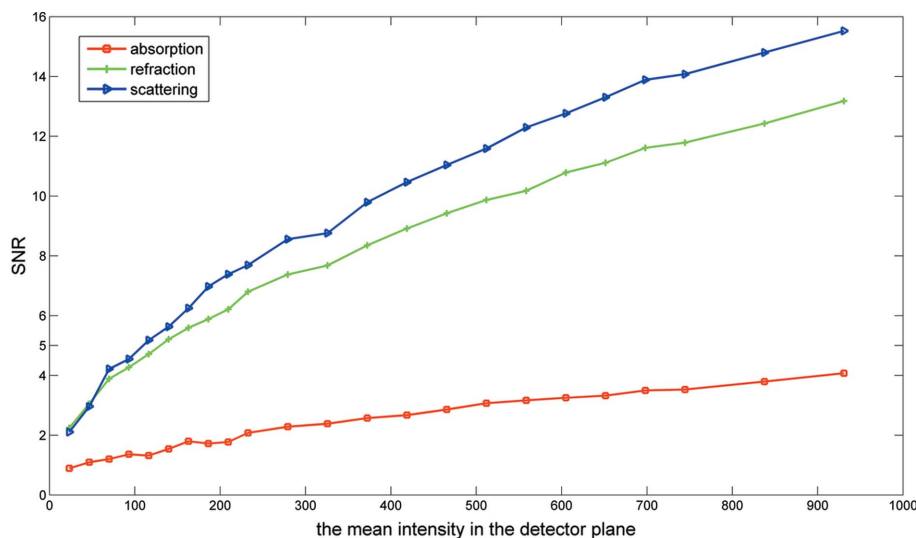
and the SNR of the refraction angle signal is higher than the absorption signal. However, this conclusion does not apply to the fourth case. Actually the fourth case often occurs when using a complex thick sample, and it will lead to the SNR of the refraction angle signal usually being smaller than that of the absorption signal. Specifically, the SNR result cannot distinguish the first case and the fourth case when the average refraction angle is zero since the positive refraction angle and the negative refractive angle cancel each other out. However, these problems will be solved using a computed tomography (CT) system, in which the SNR of the reconstructed refractive

index decrement will always be much higher than that of the reconstructed absorption coefficient. Meanwhile, since the real part and imaginary part of the refractive index are both three-dimensional functions, the SNR result of two-dimensional projection imaging is limited to be extended to three-dimensional imaging. Therefore, three-dimensional phase contrast imaging is needed to show the huge advantages of the phase contrast signal on the contrast and SNR.

The noise model we discussed takes into account photon number fluctuations of the source. Actually, though negligible in most cases, some other factors such as dark noise, analyzer

crystal jitter, imperfect crystals and thermal instabilities also contribute to the degradation of the image quality for particular designs or experimental conditions. Practical solutions such as gain correction, optimized mechanical design and temperature control can be implemented to minimize these contributions.

A set of experimental data has been collected to verify expressions of the noise variances of the extracted information. The noise properties of DEI calculated by CFR closely resemble those by maximum likelihood estimate (MLE) (Brankov *et al.*, 2004). It is noteworthy that they are also similar to the results of grating-based differential phase contrast imaging by using both the phase stepping (PS) method (Weber

**Figure 8**

SNR of different images at the edge of the sample *versus* the mean intensity in the detector plane.

et al., 2011a) and the reverse projection (RP) method (Zhu *et al.*, 2010; Wu *et al.*, 2015). CFR makes use of the similar imaging equations already derived for GDPCI, and results obtained with CFR are quantitatively comparable with MIR, thus providing a good experimental and simulated verification of the formal and practical analogies between analyzer-based imaging and grating interferometry. Actually, these results indicate that GDPCI itself is an analyzer-based imaging method. The similarity of the two phase contrast imaging methods is not surprising as they are both sensitive to the same physical quantities: the refraction angle and the refractive scattering angle. This would potentially offer a way to quantitatively compare DEI and GDPCI in a way that has not been done so far. Inspired by CFR used in DEI, and given that the phase-stepping curve in GDPCI is more suitable to be fitted by a cosine function, we will apply CFR in GDPCI to further demonstrate the applicability of the angular signal response imaging prototype in future research. Moreover, CFR can be further extended to samples with negligible scattering, where only two images are needed to separate the absorption and refraction signal, while the PS method needs at least three images to fit the object PS curve, thus reducing the radiation dose.

As a future improvement of the presented algorithm, it is also capable of obtaining simultaneously the three measured images if three analyzer crystals corresponding to the up-slope, the peak and the down-slope positions are used and monochromatic radiation scans the sample. The potential of the method offers really new opportunities, in particular in medical and biological research where the reduction of the dose and an improvement of the imaging efficiency are probably the main issues of real applications. However, the scattering model adopted in this manuscript does not consider the X-ray extinction, a phenomenon that may cause an apparent correlation between absorption and scattering. The contribution will be discussed in a forthcoming paper.

6. Conclusion

Based on the angular signal response function prototype, we analysed and calculated the noise properties of DEI. Cosine fitting radiography has been validated by Monte Carlo simulations and experimental data that show good agreement with each other. Results point out that the SNR of refraction and scattering images in DEI are about one order of magnitude better than in an absorption image at the edges of low-Z samples. By increasing photon flux and visibility the noise penalty is drastically reduced. Moreover, the analysis indicates that the advantages of phase contrast imaging will be reflected in projection imaging with thin-enough samples and three-dimensional CT imaging with complex thick samples. Generally, the experimental and simulated demonstration of the applicability of the novel algorithm to the DEI setup provides a very interesting correlation between DEI and GDPCI and is widely suitable for a variety of measurement noises in the angular signal response imaging prototype. It will be a

promising approach as less-perfect systems tend to be more practical systems that can be used in the clinic in the future.

APPENDIX A

In DEI, the noise variances derived from the photon fluctuations are

$$\sigma_T^2 = \sum_{k=\{U, P, D\}} \left(\frac{\partial T}{\partial I_k} \right)_{I_k=\bar{I}_k}^2 \sigma_{I_k}^2 = \frac{\bar{I}_D + \bar{I}_U}{(2I_0At\bar{R})^2}, \quad (27)$$

$$\begin{aligned} \sigma_\varphi^2 &= \left(\frac{\partial \tan \varphi}{\partial \varphi} \right)_{\varphi=\bar{\varphi}}^{-2} \sigma_{\tan \varphi}^2 = \cos^4 \bar{\varphi} \sum_{k=\{U, P, D\}} \left(\frac{\partial \tan \varphi}{\partial I_k} \right)_{I_k=\bar{I}_k}^2 \sigma_{I_k}^2 \\ &= (1 + \tan^2 \bar{\varphi})^{-2} \left\{ \left[\frac{-2(\bar{I}_P - \bar{I}_D)}{(2\bar{I}_P - \bar{I}_D - \bar{I}_U)^2} \right]^2 \bar{I}_U \right. \\ &\quad \left. + \left[\frac{-2(\bar{I}_D - \bar{I}_U)}{(2\bar{I}_P - \bar{I}_D - \bar{I}_U)^2} \right]^2 \bar{I}_P + \left[\frac{-2(\bar{I}_P - \bar{I}_U)}{(2\bar{I}_P - \bar{I}_D - \bar{I}_U)^2} \right]^2 \bar{I}_D \right\} \\ &= 4 \frac{(\bar{I}_P - \bar{I}_D)^2 \bar{I}_U + (\bar{I}_D - \bar{I}_U)^2 \bar{I}_P + (\bar{I}_P - \bar{I}_U)^2 \bar{I}_D}{[(2\bar{I}_P - \bar{I}_D - \bar{I}_U)^2 + (\bar{I}_D - \bar{I}_U)^2]. \quad (28)} \end{aligned}$$

Here, $\varphi(x, y) = (\pi/\theta_D) \theta_x(x, y)$, where θ_D is the Darwin width,

$$\begin{aligned} \sigma_{v_s^2}^2 &= \sum_{k=\{U, P, D\}} \left(\frac{\partial v_s^2}{\partial I_k} \right)_{I_k=\bar{I}_k}^2 \sigma_{I_k}^2 \\ &= \sum_{k=\{U, P, D\}} \left[-2 \left(\frac{\theta_D}{\pi} \right)^2 \frac{1}{V(x, y)} \frac{\partial V}{\partial I_k} \right]_{I_k=\bar{I}_k}^2 \sigma_{I_k}^2 \\ &= \frac{4\theta_d^4 4\bar{I}_P^4 - 3\bar{I}_P^2 (\bar{I}_D + \bar{I}_U)^2 + \bar{I}_P (\bar{I}_D + \bar{I}_U)^3 + \bar{I}_U \bar{I}_D (\bar{I}_D - \bar{I}_U)^2}{\pi^4 (\bar{I}_D + \bar{I}_U) \left[(2\bar{I}_P - \bar{I}_D - \bar{I}_U)^2 + (\bar{I}_D - \bar{I}_U)^2 \right]^2}. \quad (29) \end{aligned}$$

From (27), (28) and (29), one may write

$$\bar{I}_P - \bar{I}_D = I_0 At \bar{R} \exp[-M(x, y)] V(x, y) (\cos \bar{\varphi} - \sin \bar{\varphi}), \quad (30)$$

$$\bar{I}_D - \bar{I}_U = 2I_0 At \bar{R} \exp[-M(x, y)] V(x, y) \sin \bar{\varphi}, \quad (31)$$

$$\bar{I}_P - \bar{I}_U = I_0 At \bar{R} \exp[-M(x, y)] V(x, y) (\cos \bar{\varphi} + \sin \bar{\varphi}). \quad (32)$$

Taking (30), (31) and (32), after mathematical manipulations (27), (28) and (29) can be simplified as

$$\sigma_T^2 = \frac{\exp(-M)}{2I_0 At \bar{R}}, \quad (33)$$

$$\sigma_\varphi^2 = \frac{1 + 2 \sin^2 \bar{\varphi} + 2V \sin \bar{\varphi} \sin(2\bar{\varphi})}{2I_0 At \bar{R} \exp(-M) V^2}, \quad (34)$$

$$\sigma_{v_s^2}^2 = 2 \frac{\theta_D^4 4V \cos^3 \bar{\varphi} + 2(1 + V^2) \cos^2 \bar{\varphi} + 1 - V^2}{\pi^4 I_0 At \bar{R} \exp(-M) V^2}. \quad (35)$$

Acknowledgements

The authors would like to thank Professor Augusto Marcelli for his great help in the manuscript revision. This work was

partly supported by the National Basic Research Program of China (2012CB825800), the Science Fund for Creative Research Groups, NSFC (11321503), the Knowledge Innovation Program of the Chinese Academy of Sciences (KJCX2-YW-N42, Y4545320Y2) and the National Natural Science Foundation of China (NSFC 11475170, 11205157, 11305173, 11205189, 11375225 and U1332109).

References

- Agostinelli, S. *et al.* (2003). *Nucl. Instrum. Methods Phys. Res. A*, **506**, 250–303.
- Allison, J. *et al.* (2006). *IEEE Trans. Nucl. Sci.* **53**, 270–278.
- Brankov, J. G., Sáiz-Herranz, A. & Wernick, M. N. (2004). *IEEE International Symposium on Biomedical Imaging: Nano to Macro 2004*, pp. 1428–1431. IEEE.
- Bravin, A. (2003). *J. Phys. D*, **36**, A24–A29.
- Bushberg, J. T. & Boone, J. M. (2011). *The Essential Physics of Medical Imaging*. Lippincott Williams and Wilkins.
- Chapman, D., Thomlinson, W., Johnston, R., Washburn, D., Pisano, E., Gmür, N., Zhong, Z., Menk, R., Arfelli, F. & Sayers, D. (1997). *Phys. Med. Biol.* **42**, 2015–2025.
- Chen, G.-H., Zambelli, J., Li, K., Bevins, N. & Qi, Z. (2011). *Med. Phys.* **38**, 584–588.
- Chou, C.-Y., Anastasio, M. A., Brankov, J. G., Wernick, M. N., Brey, E. M., Connor, D. M. Jr & Zhong, Z. (2007). *Phys. Med. Biol.* **52**, 1923–1945.
- Diemoz, P., Bravin, A., Langer, M. & Coan, P. (2012). *Opt. Express*, **20**, 27670–27690.
- Diemoz, P. C., Coan, P., Glaser, C. & Bravin, A. (2010). *Opt. Express*, **18**, 3494–3509.
- Förster, E., Goetz, K. & Zaumseil, P. (1980). *Krist. Techn.* **15**, 937–945.
- Hall, M. M., Veeraraghavan, V. G., Rubin, H. & Winchell, P. G. (1977). *J. Appl. Cryst.* **10**, 66–68.
- Jensen, T. H., Bech, M., Zanette, I., Weitkamp, T., David, C., Deyhle, H., Rutishauser, S., Reznikova, E., Mohr, J., Feidenhans'l, R. & Pfeiffer, F. (2010). *Phys. Rev. B*, **82**, 214103.
- Khelashvili, G., Brankov, J. G., Chapman, D., Anastasio, M. A., Yang, Y., Zhong, Z. & Wernick, M. N. (2006). *Phys. Med. Biol.* **51**, 221–236.
- Kitchen, M. J., Paganin, D. M., Uesugi, K., Allison, B. J., Lewis, R. A., Hooper, S. B. & Pavlov, K. M. (2010). *Opt. Express*, **18**, 19994–20012.
- Kitchen, M. J., Pavlov, K. M., Siu, K. K. W., Menk, R. H., Tromba, G. & Lewis, R. A. (2007). *Phys. Med. Biol.* **52**, 4171–4187.
- Li, K., Bevins, N., Zambelli, J. & Chen, G. H. (2013). *Med. Phys.* **40**, 021908.
- Majidi, K., Li, J., Muehleman, C. & Brankov, J. G. (2014). *Phys. Med. Biol.* **59**, 1877–1897.
- Marquet, B., Brankov, J. G. & Wernick, M. N. (2006). *3rd IEEE International Symposium on Biomedical Imaging: Nano to Macro 2006*, pp. 1232–1235. IEEE.
- Munro, P. R. & Olivo, A. (2013). *Phys. Rev. A*, **87**, 053838.
- Nesterets, Ya. I., Coan, P., Gureyev, T. E., Bravin, A., Cloetens, P. & Wilkins, S. W. (2006). *Acta Cryst. A* **62**, 296–308.
- Oltulu, O. (2003). *A unified approach to X-ray absorption-refraction-extinction contrast with diffraction-enhanced imaging*. PhD thesis, Illinois Institute of Technology, USA.
- Pagot, E., Cloetens, P., Fiedler, S., Bravin, A., Coan, P., Baruchel, J., Härtwig, J. & Thomlinson, W. (2003). *Appl. Phys. Lett.* **82**, 3421–3423.
- Pagot, E., Fiedler, S., Cloetens, P., Bravin, A., Coan, P., Fezzaa, K., Baruchel, J., Härtwig, J., von Smitten, K., Leidenius, M., Karjalainen-Lindsberg, M. L. & Keyriläinen, J. (2005). *Phys. Med. Biol.* **50**, 709–724.
- Pelliccia, D., Rigon, L., Arfelli, F., Menk, R.-H., Bukreeva, I. & Cedola, A. (2013). *Opt. Express*, **21**, 19401–19411.
- Pfeiffer, F., Bech, M., Bunk, O., Kraft, P., Eikenberry, E. F., Brönnimann, C., Grünzweig, C. & David, C. (2008). *Nat. Mater.* **7**, 134–137.
- Revol, V., Kottler, C., Kaufmann, R., Straumann, U. & Urban, C. (2010). *Rev. Sci. Instrum.* **81**, 073709.
- Rigon, L., Arfelli, F. & Menk, R.-H. (2007a). *Appl. Phys. Lett.* **90**, 114102.
- Rigon, L., Arfelli, F. & Menk, R.-H. (2007b). *J. Phys. D*, **40**, 3077.
- Rigon, L., Besch, H.-J., Arfelli, F., Menk, R.-H., Heitner, G. & Plotnow-Besch, H. (2003). *J. Phys. D*, **36**, A107–A112.
- Rizzi, J., Mercère, P., Idir, M., Silva, P. D., Vincent, G. & Primot, J. (2013). *Opt. Express*, **21**, 17340–17351.
- Sumitani, K., Ishiji, K., Kawamoto, M., Yoneyama, A., Tabata, M., Okajima, T. & Hirai, Y. (2013). *J. Phys. Conf. Ser.* **425**, 1090.
- Tang, X. Y., Yang, Y. & Tang, S. J. (2011). *Med. Phys.* **38**, 4386–4395.
- Tang, X. Y., Yang, Y. & Tang, S. J. (2012). *Med. Phys.* **39**, 4467–4482.
- Thomlinson, W., Suortti, P. & Chapman, D. (2005). *Nucl. Instrum. Methods Phys. Res. A*, **543**, 288–296.
- Wang, Z., Huang, Z., Zhang, L., Chen, Z. & Kang, K. (2009b). *Nucl. Sci. Symp. Conf. Rec. (NSS/MIC)*, pp. 2395–2398. IEEE.
- Wang, Z.-T., Kang, K.-J., Huang, Z.-F. & Chen, Z.-Q. (2009a). *Appl. Phys. Lett.* **95**, 094105.
- Weber, T., Bartl, P., Bayer, F., Durst, J., Haas, W., Michel, T., Ritter, A. & Anton, G. (2011a). *Med. Phys.* **38**, 4133–4140.
- Weber, T., Bartl, P., Durst, J., Haas, W., Michel, T., Ritter, A. & Anton, G. (2011b). *Nucl. Instrum. Methods Phys. Res. A*, **648**, S273–S275.
- Wernick, M. N., Wirjadi, O., Chapman, D., Zhong, Z., Galatsanos, N. P., Yang, Y., Brankov, J. G., Oltulu, O., Anastasio, M. A. & Muehleman, C. (2003). *Phys. Med. Biol.* **48**, 3875–3895.
- Wu, Z., Gao, K., Chen, J., Wang, D., Wang, S., Chen, H., Bao, Y., Shao, Q., Wang, Z., Zhang, K., Zhu, P. & Wu, Z. (2015). *Med. Phys.* **42**, 741–749.
- Zhang, K., Zhu, P., Yuan, Q., Huang, W., Liu, X., Hong, Y., Gao, G., Ge, X., Wang, Z. & Wu, Z. (2010). *Anal. Bioanal. Chem.* **397**, 2067–2078.
- Zhao, X., Zhang, K., Hong, Y., Huang, W., Yuan, Q., Zhu, P. & Wu, Z. (2013). *Acta Phys. Sin.* **62**, 124202 (in Chinese).
- Zhu, P., Wang, J., Yuan, Q., Huang, W., Shu, H., Gao, B., Hu, T. & Wu, Z. (2005). *Appl. Phys. Lett.* **87**, 264101.
- Zhu, P., Yuan, Q., Huang, W., Wang, J., Shu, H., Wu, Z. & Xian, D. (2006). *Acta Phys. Sin.* **55**, 1089 (in Chinese).
- Zhu, P., Zhang, K., Wang, Z., Liu, Y., Liu, X., Wu, Z., McDonald, S. A., Marone, F. & Stampanoni, M. (2010). *Proc. Natl Acad. Sci. USA*, **107**, 13576–13581.
- Zhu, P., Zhu, Z., Hong, Y., Zhang, K., Huang, W., Yuan, Q., Zhao, X., Ju, Z., Wu, Z., Wei, Z., Wiebe, S. & Chapman, L. D. (2014). *Appl. Opt.* **53**, 861–867.